

A multi-wavelength study of $z = 3.15$ Lyman- α emitters in the GOODS South Field ^{*}

K.K. Nilsson^{1,2}, P. Møller¹, O. Möller³, J. P. U. Fynbo², M.J. Michałowski², D. Watson², C. Ledoux⁴, P. Rosati¹, K. Pedersen², and L.F. Grove²

¹ European Southern Observatory, Karl-Schwarzschild-Straße 2, 85748 Garching bei München, Germany

² Dark Cosmology Centre, Niels Bohr Institute, University of Copenhagen, Juliane Maries Vej 30, 2100 Copenhagen Ø, Denmark

³ Max-Planck-Institut für Astrophysik, Karl-Schwarzschild-Straße 1, 85741 Garching bei München, Germany

⁴ European Southern Observatory, Alonso de Córdova 3107, Casilla 19001, Vitacura, Santiago 19, Chile

Received date / Accepted date

ABSTRACT

Context. Ly α -emitters have proven to be excellent probes of faint, star-forming galaxies in the high redshift universe. However, although the sample of known emitters is increasingly growing, their nature (e.g. stellar masses, ages, metallicities, star-formation rates) is still poorly constrained.

Aims. We aim to study the nature of Ly α -emitters, to find the properties of a typical Ly α -emitting galaxy and to compare these properties with the properties of other galaxies at similar redshift, in particular Lyman-break galaxies.

Methods. We have performed narrow-band imaging at the VLT, focused on Ly α at redshift $z \approx 3.15$, in the GOODS-S field. We have identified a sample of Ly α -emitting candidates, and we have studied their Spectral Energy Distributions (SEDs).

Results. We find that the emitters are best fit by an SED with low metallicity ($Z/Z_{\odot} = 0.005$), low dust extinction ($A_V \approx 0.32$) and medium stellar masses of approximately $10^9 M_{\odot}$. The age is not very well constrained. One object out of 24 appears to be a high redshift Ly α -emitting dusty starburst galaxy. We find filamentary structure as traced by the Ly α -emitters at the 4σ level. The rest-frame UV SED of these galaxies is very similar to that of Lyman Break Galaxies (LBGs) and comply with the selection criteria for U -band drop-outs, except they are intrinsically fainter than the current limit for LBGs.

Conclusions. Ly α -emitters are excellent probes of galaxies in the distant universe, and represent a class of star-forming, dust and AGN free, medium mass objects.

Key words. cosmology: observations – galaxies: high redshift

1. Introduction

The possibility to use the Ly α emission line to study galaxies in early stages of their formation was outlined already by Partridge & Peebles (1967) nearly 40 years ago, but early surveys (see Pritchett 1994 for a review) failed to produce anything other than upper limits. The unexpected faintness of the objects caused it to take almost three decades before the narrow-band technique was successfully used to identify the first high redshift Ly α emitting galaxies that were not dominated by Active Galactic Nuclei (e.g., Lowenthal et al. 1991; Möller & Warren 1993; Hu & McMahon 1996; Petitjean et al. 1996; Francis et al. 1996; Cowie & Hu 1998). It is only recently, with the advent of 8 m class telescopes and sensitive detectors, that larger samples of Ly α selected objects have been reported (e.g. Steidel et al. 2000; Malhotra & Rhoads 2002; Fynbo et al. 2003; Ouchi et al. 2003; Hayashino et al. 2004; Venemans et al. 2005).

Already during the early studies, two interesting suggestions were raised. First, it was found that there is a tendency for Ly α

selected objects to “line up” as strings in redshift space, and that they therefore may be excellent tracers of filaments at high redshifts (Warren & Møller 1996; Ouchi et al. 2004; Matsuda et al. 2005). Secondly, they were found to have very faint broad band magnitudes and therefore could be good tools in detecting faint, high redshift galaxies (Fynbo et al. 2001; Fujita et al. 2003; Venemans et al. 2005; Gawiser et al. 2006).

The first of those suggestions was explored theoretically via modelling of structure formation including assignment of Ly α emission to the models (Furlanetto et al. 2003; Monaco et al. 2005), and has been confirmed observationally (Møller & Fynbo 2001; Hayashino et al. 2004), who also proposed to use such structures for a new cosmological test to measure Ω_{Λ} by looking at the “length-to-radius” ratio of filaments observed from the side or end-on. This proposed test was subsequently explored in detail by Weidinger et al. (2002).

The second suggestion has gained significant interest because there are now several additional, but independent, ways of identifying high redshift but optically faint galaxies, e.g. Damped Ly α Absorbers (DLA) galaxies (Wolfe et al. 1986; Møller et al. 2002; Wolfe, Gawiser & Prochaska 2005), Gamma-Ray Burst (GRB) host galaxies (Fruchter et al. 2006), sub-mm galaxies (Chapman et al. 2004). Most galaxies from such

Send offprint requests to: kim@dark-cosmology.dk

^{*} Based on observations carried out at the European Southern Observatory (ESO) under prog. ID No. 70.A-0447, 274.A-5029 and LP168.A-0485.

searches are however too faint to be identified in current ground-based optical flux limited samples. A significant project (the Building the Bridge Survey, BBS) aimed at addressing those issues is currently underway at the ESO Very Large Telescope (VLT) (Fynbo et al. 2001; Fynbo et al. 2003). The very faintness of the objects, however, renders it difficult to make any detailed comparisons. While some DLA galaxies have been imaged with HST (Warren et al. 2001; Møller et al. 2002) and likewise GRB hosts (Jaunsen et al. 2003; Fynbo et al. 2005), and sub-mm galaxies (Smail et al. 2004; Pope et al. 2005; Schmitt et al. 2006), only a very small subset of the Ly α selected galaxies have been imaged with HST (Pascarella et al. 1996; Venemans et al. 2005; Overzier et al. 2006) and furthermore, such images are mostly too shallow for a detailed study.

The GOODS-S (Giavalisco et al. 2004) provides a unique opportunity to obtain a deep, high resolution, multi-band data set of a complete and unbiased sample of Ly α -emitters (or LEGOs for Ly α Emitting Galaxy-building Objects; Møller & Fynbo (2001)). We have therefore started a program to collect a complete, unbiased sample of LEGOs in the GOODS-S. This allows a detailed study of the global properties, e.g. photometry and morphology of LEGOs, as well as SED fits including photometry from the large, available multi-wavelength data-set.

This paper is organised as follows; in section 2 we present the imaging observations, data reductions and candidate selection process. In section 3 we present spectroscopic observations of three candidates as well as the results from these observations. Sections 4, 5 and 6 contain the discussion of various aspects of the LEGO candidate sample; first the basic characteristics of the LEGO sample, then the SED fitting and finally a comparison to Lyman-Break Galaxies. The conclusion is presented in section 7.

Throughout this paper, we assume a cosmology with $H_0 = 72 \text{ km s}^{-1} \text{ Mpc}^{-1}$ (Freedman et al. 2001), $\Omega_m = 0.3$ and $\Omega_\Lambda = 0.7$. Magnitudes are given in the AB system. We survey a comoving volume of $\approx 3300 \text{ Mpc}^3$.

2. Imaging

2.1. Narrow band observations and data reduction

A $400 \times 400 \text{ arcsec}^2$ section of the GOODS-S field centred on R.A. = $03^h 32^m 21.9^s$ and Dec = $-27^\circ 45' 50''.7$ (J2000) was observed with FORS1 on the VLT 8.2 m telescope Antu during two visitor mode nights on December 1-3, 2002. The log of observations is given in Table 1. A total of 16 dithered exposures were obtained over the two nights for a combined exposure time of 30000 seconds, all with the narrow band filter OIII/3000+51 and using the standard resolution collimator ($0.2 \times 0.2 \text{ arcsec}^2$ pixels). For this setup the central wavelength of the filter is 505.3 nm with a FWHM of 5.9 nm which corresponds to the redshift range $z = 3.131 - 3.180$ for Ly α . The transmission curve of the filter is shown in Fig. 1. The four spectrophotometric standards Feige110, LDS749B, LTT3864, and LTT3218 were observed on the same nights.

The observing conditions were unstable during the two nights with the seeing FWHM, as measured on the images, varying between $0''.66$ and $1''.25$ on the first night and between $1''.4$ and $3''.3$ on the second night. The images were reduced (de-biased and corrected for CCD pixel-to-pixel variations) using standard techniques. The individual reduced images were combined using a modified version of our code that optimises the Signal-to-Noise (S/N) ratio for faint, sky-dominated sources (see

Møller & Warren, 1993, for details on this code). The 5σ detection limit of the combined narrow-band image as measured in circular apertures with radius twice the full width half maximum of point sources, i.e. with radius $1''.6$, is $\text{mag(AB)} = 26.1$. The combined narrow-band image is shown in Fig. 2.

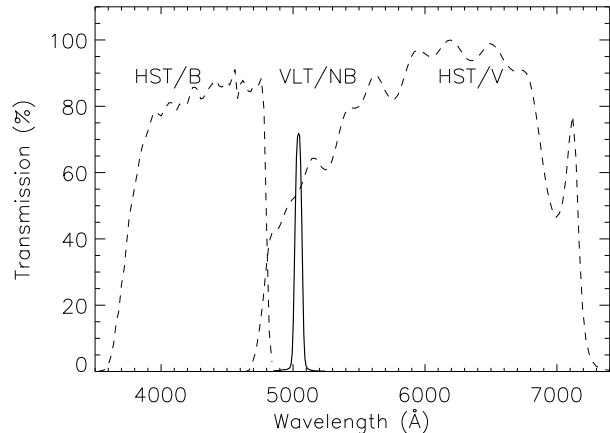


Fig. 1. Transmission of selection filters. The VLT FORS1 narrow-band filter is drawn with a solid line. Dashed lines show the HST *B* and *V* filters.

Table 1. Log of imaging observations with FORS1.

| date | total exp. | seeing range |
|---------------|------------|---------------------|
| 01-02.12.2002 | 5.54 hours | $0''.66$ - $1''.25$ |
| 02-03.12.2002 | 2.78 hours | $1''.43$ - $3''.30$ |

2.2. Selection of LEGOs in the fields

For the selection of LEGO candidates we used the narrow-band image as detection image and the HST/ACS *B*- (F435W) and *V*-band (F606W) images as selection images. The HST data is part of the public data in GOODS-S (Giavalisco et al. 2004). This selection set-up, with a broad-band filter on either side of the narrow-band filter, appears to be one of the most efficient configurations for selection of emission-line objects (Hayes & Östlin 2006; Hayes priv. communication). The HST images were re-binned to the pixel size of the narrow-band image. Due to the smaller field-of-view of the HST/ACS images, the narrow-band image was cut into six sub-images to match the size of the HST images.

Our selection method consists of three consecutive steps. First, using the software package SExtractor (Bertin & Arnouts 1996), we select all objects identified in the narrow-band image. The narrow-band image is scanned with a detection threshold equal to the background sky-noise and requiring a minimum area of 5 connected pixels above this threshold. Centred on each candidate object we then extract photometry from the narrow, *V*, and *B*-band images using identical circular apertures of $2''$ diameter. Note that through this process we make no attempt to identify broad band counterparts to the narrow band objects. The

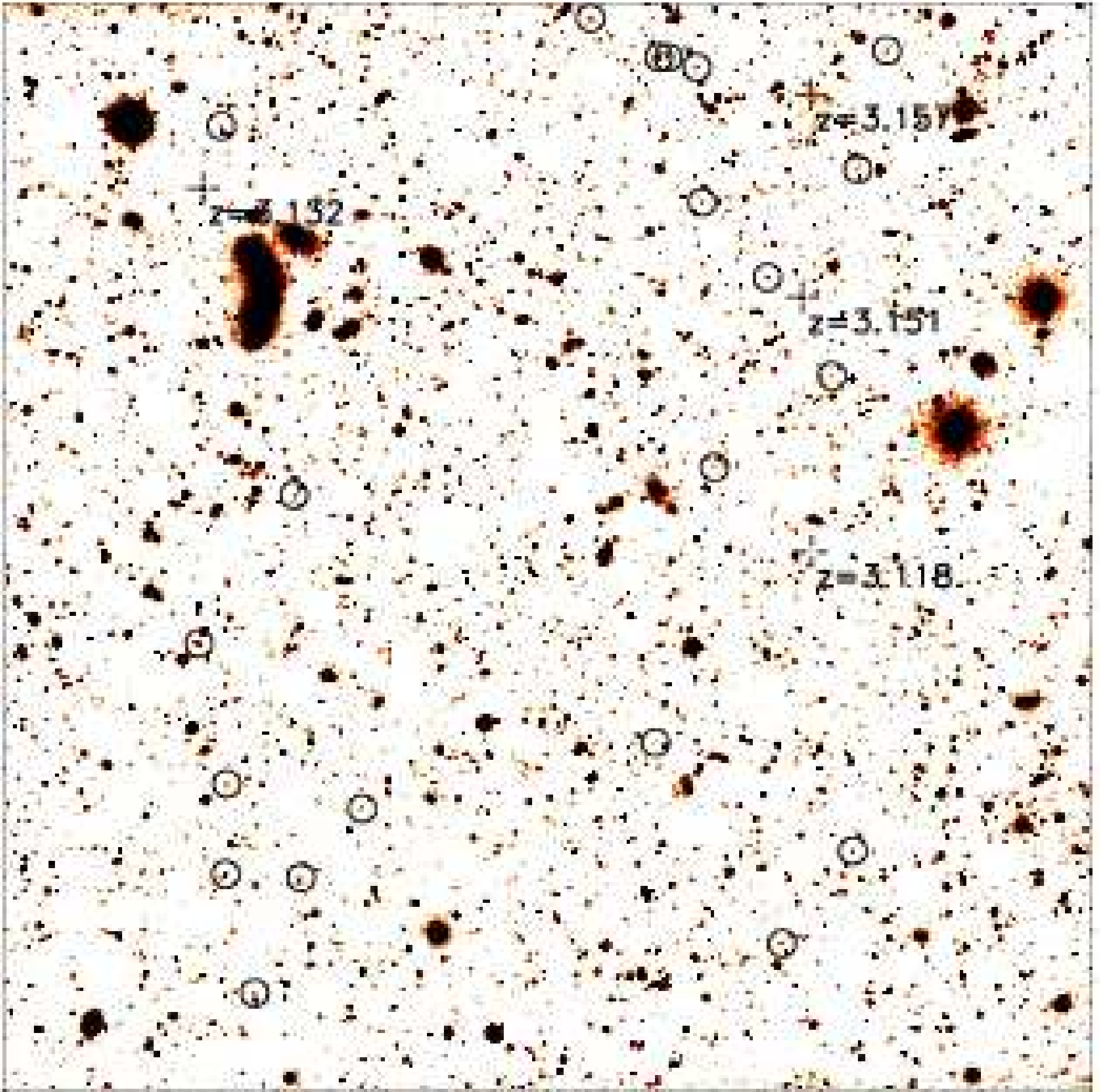


Fig. 2. The VLT/narrow-band image of the 400×400 arcsec² field with the positions of selected LEGO candidates (see Sect. 2.2) shown with circles. Spectroscopically confirmed candidates are marked with crosses and their redshifts are indicated. North is up and East is left. The right, uppermost spectroscopically confirmed candidate is the Ly α blob (Nilsson et al. 2006).

broad band photometry is extracted in apertures defined solely from the centroid positions in the narrow band image. There is always a small but finite possibility that an unrelated foreground or background object could fall inside the $2''$ aperture which would complicate the search for emission line objects. This complication is minimised by not re-centering the aperture on objects in the broad band images.

The second step is to accept only candidates that are detected at $S/N > 5$ in the narrow band circular aperture and are found at least 20 pixels from the edge of each image. This leaves us with a catalogue of 2616 narrow band objects within the resulting $385 \times$

400 arcsec² field. The term “narrow band objects” is used here only to underline that while they are 5σ detections in the narrow band image, they may or may not have been detected in the broad band images.

In the third step we select the subset of our catalogue comprising of potential emission line objects. Via interpolation of the flux levels in the B and V bands it is easy to calculate the continuum flux at the central wavelength of the narrow band filter, and from there to obtain the equivalent width (EW) of a potential line and its associated propagated statistical error. Note that we here calculate the “EW of the aperture”, which means that

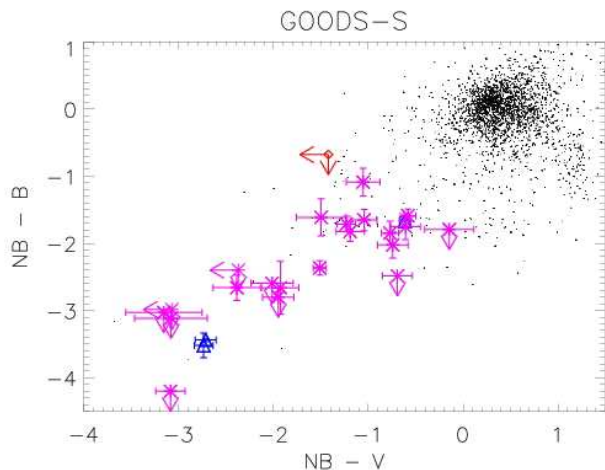


Fig. 3. Colour-colour plot. Dots mark the whole sample of 2616 objects selected with SExtractor. Points with errors mark the selected emission-line objects. Stars (in magenta) mark the candidate sample, the triangles (in blue) the spectroscopically confirmed LEGOs and the open diamond (in red) the blob (Nilsson et al., 2006). Dots detected in the same region of the plot as the selected sample, but that are not selected, consist of objects that were discarded in the visual inspection.

if there is only one object in the aperture, then we find the EW of that object. If there are additional unrelated neighbours inside the aperture, then the calculated EW will be smaller than the actual EW. Our listed EWs (see Table 2) are in that sense conservative lower limits. For the present work we are interested only in those with positive values of EW (emission line objects), and only the subset of those where the significance of the line is high enough to provide a high probability that it is reliable, i.e. providing a high efficiency of spectroscopic follow-up work. For the current field we already have a few spectroscopic confirmations (see Sec. 3) and we conservatively chose to cut at the EW significance level (2.9σ) where all confirmed LEGOs are included. This corresponds to a formal probability of 99.6% for confirmation of each object and we find 106 such objects. Of these, three are associated with a Ly α -blob that we found in this field (Nilsson et al., 2006). Ly α -blobs (e.g. Fynbo et al. 1999; Steidel et al. 2000; Matsuda et al. 2004) are large luminous nebulae, with sizes up to 150 kpc, emitting solely Ly α emission. The Ly α luminosity can reach 10^{43} erg s $^{-1}$. 79 of the 106 objects with EW excess are ruled out after visual inspection due to stellar artefacts, saturated sources or for lying on parts of the image where the HST sky background is poorly constrained. Thus, we are finally left with a sample of 24 LEGO candidates. These candidates are presented in Table 2. The formal probability of 99.6% for confirmation of the emission line results in 0.10 spurious detections in our sample of 24 objects. A colour-colour plot of the narrow-band sources can be found in Fig. 3.

2.3. Continuum counterparts and final photometry

Following the selection process outlined above, we examined the narrow-band and broad-band images to find continuum counterparts to the narrow-band objects. The process of finding counterparts to the narrow-band objects is complicated by the very different PSF characteristics of the narrow- and broad-band im-

Table 2. Data on first selection. Coordinates are in J2000. Equivalent widths are calculated from the “first selection”, i.e. with $2''$ radius apertures, centred on the narrow-band source centroid, see section 2.2.

| S/N is the signal-to-noise of the equivalent width. | | | | | |
|---|--------------------------|----------------------|-----|-------------|-------------|
| LEGO GOODS-S | EW _{obs} (Å) | σ_{EW} (Å) | S/N | R.A. | Dec |
| 1 | 896 | 57 | 16 | 03:32:14.83 | -27:44:17.5 |
| 2 | 59 | 15 | 3.8 | 03:32:17.62 | -27:43:42.3 |
| 3 | 172 | 24 | 7.1 | 03:32:18.56 | -27:42:48.4 |
| 4 | 901 | 48 | 19 | 03:32:31.46 | -27:43:37.2 |
| 5 | 184 | 30 | 6.0 | 03:32:30.02 | -27:48:37.1 |
| 6 | 517 | 23 | 22 | 03:32:30.82 | -27:47:52.8 |
| 7 | 153 | 32 | 4.7 | 03:32:13.40 | -27:47:43.9 |
| 8 | 85 | 20 | 4.3 | 03:32:30.79 | -27:47:19.2 |
| 9 | 100 | 24 | 4.2 | 03:32:12.49 | -27:42:45.8 |
| 10 | 52 | 16 | 3.3 | 03:32:13.30 | -27:43:29.9 |
| 11 | 154 | 33 | 4.6 | 03:32:27.03 | -27:47:28.3 |
| 12 | 151 | 33 | 4.6 | 03:32:13.99 | -27:44:47.0 |
| 13 | 53 | 18 | 2.9 | 03:32:14.58 | -27:45:52.5 |
| 14 | 37 | 4 | 8.3 | 03:32:18.82 | -27:42:48.3 |
| 15 | 88 | 11 | 7.9 | 03:32:31.56 | -27:46:26.9 |
| 16 | 34 | 7.5 | 4.4 | 03:32:20.72 | -27:42:33.8 |
| 17 | 202 | 46 | 4.4 | 03:32:28.93 | -27:45:31.5 |
| 18 | 269 | 55 | 4.9 | 03:32:17.26 | -27:45:21.0 |
| 19 | 47 | 12 | 3.9 | 03:32:15.80 | -27:44:10.3 |
| 20 | 58 | 15 | 3.9 | 03:32:30.96 | -27:43:14.2 |
| 21 | 53 | 16 | 3.4 | 03:32:28.73 | -27:47:54.1 |
| 22 | 58 | 15 | 4.0 | 03:32:17.77 | -27:42:52.1 |
| 23 | 362 | 57 | 6.3 | 03:32:15.37 | -27:48:18.5 |
| 24 | 136 | 24 | 5.7 | 03:32:18.89 | -27:47:03.6 |

ages. This is illustrated in Fig. 4. For some of the candidates, no obvious counterpart was detected, but rather several counterpart candidates were found with small offsets. To determine what continuum objects were associated with the narrow-band source, two co-authors separately inspected the images visually. If only one counterpart was in the vicinity of the centroid of the narrow-band source, this object was identified as sole counterpart. If several sources were detected, their magnitudes were measured and the statistical probability that they would appear in the area surrounding the narrow-band centroid was evaluated from number counts of galaxy searches. We then separately determined which counterparts we considered credible counterparts, and the lists were compared. Only counterparts assigned by both authors were accepted as counterparts. This yielded 2 LEGO candidates without counterparts, 14 candidates with single counterparts and 8 LEGOs with two or more counterparts. Aperture photometry was then performed on all candidates in the narrow-band and their selected counterparts in the HST broad band images. We used aperture radii of two times the FWHM of each image. Aperture corrections were calculated for each image for point sources (see Table 5). For candidates where multiple components were assigned, small apertures were placed either *i*) centred on each counterpart separately if the counterparts are further apart than two times the radius of the aperture, *ii*) centred on a coordinate half way between the counterparts if the distance between counterparts is less than one times the radius of the aperture or *iii*) apertures slightly shifted from the central coordinate of the counterparts to ensure that different apertures do not overlap if the distance between counterparts is less than two, but more than one, times the aperture radius. The magnitudes, EWs and star formation rates (SFRs) for all candidates can be found in Table 3, see also Sec. 4.1. Multiple candidates

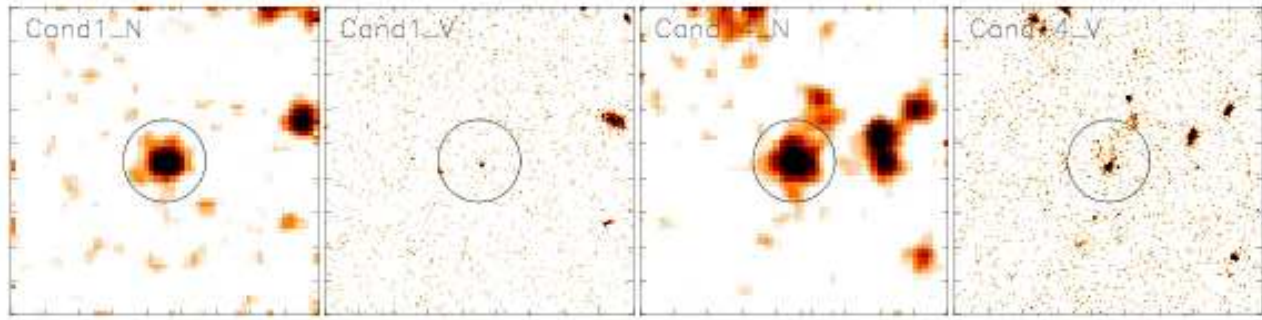


Fig. 4. In this figure, we illustrate the difficulty in determining which broad-band counterpart was associated with the narrow-band source. Images are $12''$ across and are centred on the narrow-band source. The circles mark the apertures used in the initial photometry, see section 2.2. The two left panels show a simple case with only one possible counterpart. The two right panels show a more complex case. In this case, all objects within the circle were assumed to be counterparts. In both cases a presumably unrelated object is seen at the edge of the aperture.

are marked with a star. To investigate how correct our method is for measuring fluxes of multiple objects, we also measured the photometry using larger apertures; for the six multiple counterparts with distances between the counterparts less than two times the radius of the aperture (LEGO GOODS-S_# 9, 10, 12, 14, 19 and 22), we applied new apertures with radii half of the distance between counterparts plus the original aperture radius. For five candidate counterparts, the difference in flux measured was within 1.5σ of the previously measured value. Hence we conclude that our original measurements are correct. The remaining candidate, LEGO GOODS-S_# 14, has a very complicated morphology, see also Fig. 4. For this candidate, the flux increased to $M_B = 25.49 \pm 0.11$, $M_V = 24.47 \pm 0.04$, $M_I = 24.36 \pm 0.13$ and $M_{z'} = 24.49 \pm 0.13$. This reduces the observed EW to $91 \pm 8 \text{ \AA}$.

In summary we first performed simple circular aperture photometry in order to select candidates based on our conservative emission-line definition (Table 2). For the selected candidates, we then searched for continuum counterparts in the high resolution HST images and carried out detailed final photometry where such counterparts were found. This final photometry provides the relevant magnitudes that describe the objects and is reproduced in Table 3.

3. Spectroscopy

3.1. Observations and reductions

Follow-up Multi-Object Spectroscopy (MOS) was obtained in service mode with FORS1/VLT UT2 over the time period December 2004 – February 2005. The total observing time of 5.5 hours was granted to confirm the redshift of the Ly α -blob found in this field, as published in Nilsson et al. (2006). In addition, we had the opportunity to add three of our compact emitters on the mask. The mask preparation was done using the *FORS Instrumental Mask Simulator*. Stars were placed on the remaining slits for calibration purposes. The MOS slitlets had a width of $1''.4$ and the combination of grism 600V and order sorting filter GG435 was used. The grism covers the wavelength range 4650 \AA to 7100 \AA with a resolving power of approximately 700. The seeing varied between $0''.77 - 1''.2$.

The bias subtraction, flat-fielding and wavelength calibration was performed using the FORS1 pipeline. The individual, 2-dimensional, reduced science spectra were combined using a σ -clipping for rejection of cosmic ray hits. The sky was subse-

Table 4. Names, Ly α -fluxes, redshifts and line ratios for spectroscopically confirmed LEGOs. The line ratios refer to the upper limit to the [OIII] line, if the emission line is [OII].

| LEGO_GOODS-S# | $F_{\text{Ly}\alpha}$ ($\text{erg s}^{-1} \text{ cm}^{-2}$) | z | $\log(F_{[\text{OIII}]}/F_{[\text{OII}]})$ |
|---------------|--|-------|--|
| 1 | 3.31×10^{-17} | 3.151 | < -0.62 |
| 4 | 2.79×10^{-17} | 3.132 | < -0.54 |
| 13 | 2.84×10^{-17} | 3.118 | < -0.55 |

quently subtracted with MIDAS by averaging the values of all pixels on either side of the spectrum and expanding this value to the size of the frame. One-dimensional spectra were extracted by summing the column values over the spectra. The spectra were then flux calibrated with three stars that were on our slits, by measuring the stellar fluxes in the narrow-band image in $2''$ diameter apertures and comparing to the integrated flux in the narrow-band from the 1-d spectra. Because LEGOs are often extended in Ly α (Møller & Warren 1998; Fynbo et al. 2001) they are likely to have higher Ly α fluxes than those listed in Table 4.

3.2. Results of first spectroscopic follow-up

The spectra of our three confirmed high-redshift Ly α -emitters can be found in Fig. 5. Neither candidate show any other emission lines in their spectra. To consider if the emission line could be [OII], we study line ratios compared to other lines that should be observed in such a case. In Fynbo et al. (2001), the expected line ratios of H β , [OII], [OIII] and NeII for [OII]-emitters were presented. For the spectroscopic sample, the 3σ upper limits of the ratio $\log(F_{[\text{OIII}]}/F_{[\text{OII}]})$ are given in Table 4 if the emission lines is [OII]. The limit will be the same for all other lines, as none are detected. As in Fynbo et al. (2001), we conclude that these are highly unlikely values for [OII]-emitters, and that the detected emission line is redshifted Ly α . Details from the spectroscopic follow-up is presented in Table 4.

In the following sections we analyse the entire sample of confirmed LEGOs and LEGO candidates together. We expect the contamination of low redshift emitters to be small. Our previous surveys have had spectroscopic success rates of 75 - 90 % (Fynbo et al. 2001; Fynbo et al. 2003). Hence, we expect that more than 18 of our 24 candidates are true Ly α -emitters.

Table 3. Final photometry of candidates in narrow- and broad-bands (Sec. 2.3) and observed Ly α EWs. Magnitudes are calculated using two times full width half maximum apertures, including aperture corrections, centred on each identified counterpart. Errors are 1σ , upper limits are 3σ . Equivalent widths are calculated again from the magnitudes printed in this table. Star formation rates are from the Ly α fluxes. Emitters marked in bold are spectroscopically confirmed, see Sec. 3. Candidates marked with a star have multiple counterparts. For these candidates, the total magnitude is given here.

| LEGO GOODS-S.# | M_{narrow} | M_B | M_V | M_i | $M_{z'}$ | EW _{obs,Lyα} (Å) | SFR _{Lyα} (M_{\odot}/yr) |
|-------------------|------------------------------------|------------------------------------|------------------------------------|------------------------------------|------------------------------------|---|--|
| 1 | 24.35 \pm 0.07 | 27.87 \pm 0.17 | 27.08 \pm 0.07 | 27.33 \pm 0.28 | 27.07 \pm 0.22 | 1006 \pm 71 | 3.94 \pm 0.24 |
| 2 | 25.36 \pm 0.17 | 28.02 \pm 0.35 | 27.29 \pm 0.10 | 27.39 \pm 0.26 | > 27.52 | 434 \pm 82 | 1.55 \pm 0.22 |
| 3 | 24.97 \pm 0.06 | > 28.08 | 28.05 \pm 0.38 | > 27.67 | > 27.24 | 912 \pm 52 | 2.22 \pm 0.11 |
| 4 | 24.19 \pm 0.02 | 27.63 \pm 0.02 | 26.91 \pm 0.11 | 27.25 \pm 0.30 | 27.07 \pm 0.32 | 956 \pm 15 | 4.55 \pm 0.07 |
| 5 | 25.29 \pm 0.03 | > 28.32 | 28.45 \pm 0.40 | > 28.68 | > 26.89 | 881 \pm 27 | 1.65 \pm 0.04 |
| 6 | 24.03 \pm 0.04 | > 28.23 | 27.12 \pm 0.15 | > 27.52 | > 27.31 | 1639 \pm 64 | 5.28 \pm 0.19 |
| 7 | 25.45 \pm 0.21 | > 28.05 | 27.47 \pm 0.09 | 27.34 \pm 0.28 | > 27.26 | 436 \pm 103 | 1.42 \pm 0.24 |
| 8 | 25.23 \pm 0.14 | 27.89 \pm 0.13 | 27.62 \pm 0.21 | 27.39 \pm 0.37 | > 27.37 | 532 \pm 81 | 1.74 \pm 0.21 |
| 9* | 24.75 \pm 0.08 | 26.46 \pm 0.09 | 25.98 \pm 0.06 | 25.64 \pm 0.13 | 26.03 \pm 0.15 | 169 \pm 16 | 2.73 \pm 0.18 |
| 10* | 25.02 \pm 0.12 | 26.84 \pm 0.09 | 26.21 \pm 0.09 | 26.24 \pm 0.08 | 26.50 \pm 0.20 | 179 \pm 27 | 2.13 \pm 0.22 |
| 11 | 25.28 \pm 0.16 | > 28.27 | > 28.36 | > 27.86 | > 27.60 | > 834 | 1.66 \pm 0.22 |
| 12* | 25.97 \pm 0.24 | > 27.76 | 26.11 \pm 0.09 | 27.43 \pm 0.29 | > 27.46 | 76 \pm 34 | 0.89 \pm 0.18 |
| 13 | 25.63 \pm 0.23 | 27.24 \pm 0.15 | 27.13 \pm 0.12 | 27.24 \pm 0.28 | > 27.08 | 178 \pm 57 | 1.21 \pm 0.23 |
| 14* | 23.97 \pm 0.05 | 25.64 \pm 0.05 | 24.58 \pm 0.03 | 24.39 \pm 0.04 | 24.64 \pm 0.06 | 110 \pm 8 | 5.58 \pm 0.26 |
| 15* | 24.22 \pm 0.05 | 26.59 \pm 0.09 | 25.73 \pm 0.04 | 25.25 \pm 0.04 | 25.22 \pm 0.06 | 296 \pm 18 | 4.42 \pm 0.21 |
| 16 | 24.92 \pm 0.11 | > 27.72 | 26.87 \pm 0.12 | 26.12 \pm 0.08 | 25.46 \pm 0.08 | 473 \pm 59 | 2.33 \pm 0.23 |
| 17* | 25.09 \pm 0.08 | 26.94 \pm 0.16 | 25.86 \pm 0.05 | 25.62 \pm 0.08 | 25.33 \pm 0.08 | 138 \pm 15 | 1.98 \pm 0.14 |
| 18 | 25.37 \pm 0.16 | 27.39 \pm 0.12 | 26.11 \pm 0.04 | 25.73 \pm 0.04 | 25.84 \pm 0.10 | 149 \pm 32 | 1.54 \pm 0.21 |
| 19* | 25.43 \pm 0.07 | 27.02 \pm 0.06 | 26.01 \pm 0.03 | 25.80 \pm 0.08 | 26.16 \pm 0.07 | 102 \pm 11 | 1.45 \pm 0.10 |
| 20 | 25.99 \pm 0.15 | 27.08 \pm 0.14 | 27.04 \pm 0.09 | 26.23 \pm 0.11 | 26.02 \pm 0.13 | 90 \pm 23 | 0.87 \pm 0.11 |
| 21 | 25.48 \pm 0.06 | > 27.88 | > 27.86 | > 27.44 | > 27.35 | > 443 | 1.38 \pm 0.07 |
| 22* | 25.05 \pm 0.15 | 26.80 \pm 0.12 | 25.65 \pm 0.04 | 25.65 \pm 0.08 | 25.60 \pm 0.08 | 115 \pm 26 | 2.07 \pm 0.27 |
| 23 | 25.30 \pm 0.15 | > 27.78 | 25.99 \pm 0.05 | 25.47 \pm 0.04 | 25.43 \pm 0.07 | 174 \pm 35 | 1.64 \pm 0.21 |
| 24 | 25.46 \pm 0.12 | 27.12 \pm 0.10 | 26.51 \pm 0.06 | 26.02 \pm 0.07 | 26.04 \pm 0.12 | 146 \pm 25 | 1.41 \pm 0.15 |

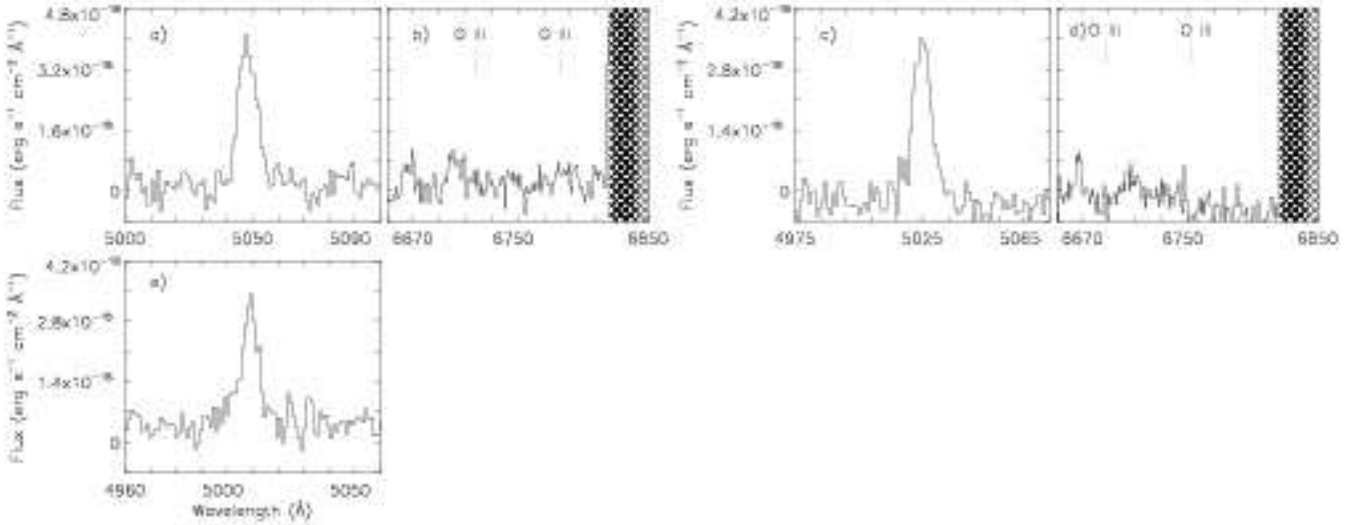


Fig. 5. Spectra of confirmed LEGOs in GOODS-S. *a)* LEGO_GOODS-S#1 emission line, *b)* LEGO_GOODS-S#1 expected position of [OIII] lines if the detected emission line is [OII], *c)* LEGO_GOODS-S#4 emission line, *d)* LEGO_GOODS-S#4 expected position of [OIII] lines if the detected emission line is [OII], *e)* LEGO_GOODS-S#13 emission line. Our spectrum did not cover the position of [OIII] if the emission line is [OII] for LEGO_GOODS-S#13. Hatched areas mark the positions of bright sky lines.

4. Basic characteristics of LEGOs

4.1. SFR, surface density and sizes

For our final sample of LEGO candidates, we calculate the star formation rate (SFR) as derived from Kennicutt (1983) by:

$$\text{SFR} = \frac{L_{\text{H}\alpha}}{1.12 \times 10^{42}} M_{\odot} \text{yr}^{-1} \quad (1)$$

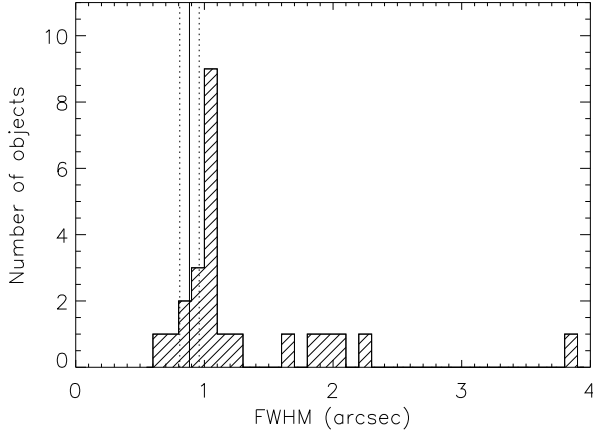


Fig. 6. Histogram plot over the size of our candidates in the narrow-band image. The bin size is 0.1 arcsec, the solid line represents the PSF of the image and the dotted lines the 1σ error on the PSF. The PSF was determined from 28 objects with SExtractor keyword CLASS_STAR greater than 0.9 and fluxes in the range of our LEGO candidates. The object in the highest FWHM bin is the GOODS-S blob (Nilsson et al., 2006).

where the $H\alpha$ luminosity, $L_{H\alpha}$, is obtained with the conversion between Ly α and $H\alpha$ luminosities of Brocklehurst (1971) of $L(\text{Ly}\alpha) = 8.7 \times L(H\alpha)$. The SFR values of the LEGO candidates can be found in Table 3. The mean SFR, as derived from the Ly α -emission for all candidates is $1.8 M_{\odot}/\text{yr}$. The total SFR is $43 M_{\odot}/\text{yr}$, yielding a star formation rate density ρ_{SFR} of $0.013 M_{\odot}/\text{yr}/\text{Mpc}^3$. This value is in very good agreement with other results for high redshift galaxies at this redshift of e.g. Madau et al. (1996; $0.016 M_{\odot}/\text{yr}/\text{Mpc}^3$), Steidel et al. (1999; $0.05 M_{\odot}/\text{yr}/\text{Mpc}^3$) and Cowie & Hu (1998; $0.01 M_{\odot}/\text{yr}/\text{Mpc}^3$). The results from Steidel et al. (1999) has been obtained from integrating the extrapolated luminosity function down to a luminosity of $0.1 L_*$, and the results are also corrected for dust by multiplying by a factor of 4.7. Hence, their results uncorrected for dust is $0.011 M_{\odot}/\text{yr}/\text{Mpc}^3$. There is very good agreement between the dust uncorrected measurements of the SFR density at $z \sim 3$.

We find a surface density of LEGOs at redshift $z = 3.15, \delta z = 0.05$ in the GOODS-S field of 0.53 objects per arcmin^2 . We can compare this with all V band sources in the GOODS-S field by extracting all sources with V band magnitudes between 25 – 28 in the available online catalogue. We find 23885 such sources in the entire GOODS-S area, covering approximately 160 arcmin^2 , corresponding to a surface density of 149 arcmin^{-2} . If we assume a homogeneous density of LEGOs between redshift 3.0 – 3.5, then the surface density of LEGOs, scaled with our candidate sample, will be $\approx 5.3 \text{ arcmin}^{-2}$. Thus, approximately 4 % of all V -detected sources with a magnitude of $V = 25 - 28$ were selected as Ly α -emitters in the redshift range $z = 3.0 - 3.5$.

We measured the sizes of our candidates in the narrow-band images using the FLUX_RADIUS option in SExtractor. This gives the half width half maximum of each source. Object LEGO_GOODS-S# 11 was excluded because it was blended with another, unrelated object. The histogram of the sizes, compared to a point source, is presented in Fig. 6. Most objects ap-

pear to be barely resolved. However, there is a tail of larger objects extending towards the GOODS-S blob. In a future paper, we will present a complete morphological study of the candidate sample.

4.2. Filamentary structure

Previous studies of Ly α emitters have reported the identification of filamentary structures (e.g. Møller & Fynbo 2001; Hayashino et al. 2004; Matsuda et al. 2005). The volume we survey here is approximately 3 times as long along the line-of-sight as it is wide which means that several filaments could be crossing the volume at different redshifts and with different position angles. If that was the case, they would likely blend together to wash out individual structures. Bearing this in mind we can still ask the question of whether the objects on our candidate list are randomly distributed across the field, or if they appear to be systematically aligned.

Inspecting Fig. 2 we note that the candidates do in fact appear to be aligned in two filamentary structures approximately along the y-axis of the CCD (oriented N-S). To investigate whether this is a significant effect, we have calculated the distances between all objects and plotted a histogram of the projected distances between all candidates in Fig. 7. The histogram shows a definite division in two components, one describing the typical width of a filament, and the other the projected distance between the filaments. To optimise the search, we calculated the angle of rotation that minimised the variance of the x-coordinates around a mean. For the two filaments, these angles are 1.75° and 2.52° respectively. For the analysis, we rotate the filament by the average, 2.13° . We then generated 10^7 uniform random sets of coordinates, with the same number of objects, and repeated the same analysis of calculating distances between pairs. To establish how reliable our observed distribution is, we perform a Kolmogorov-Smirnov test (e.g. Peacock 1983) on the simulated distributions. The test showed that the likelihood of the alignment being random is less than 2.5×10^{-4} , hence a near 4 sigma detection, see Fig. 7. We fitted a double Gaussian function to the histogram plot. This gives the typical width of the filaments as the FWHM of the first peak, and the distance between them as the mean distance to the second peak. We find that the typical width is ≈ 250 pixels, corresponding to 370 kpc at redshift 3.15, in good agreement with the findings of Møller & Fynbo (2001) who find a spectroscopically confirmed filament with 400 kpc radius from a set of Ly α -emitters at $z = 3.04$. The distance between the first and second peak is ≈ 950 pixels, corresponding to 1.4 Mpc at this redshift. To further verify this filamentary structure would require more spectroscopic data, that would also enable a 3D-plot of the filaments in space.

5. SED fitting

The imaging available in the GOODS-S field is extensive. The data, in 14 publicly available broad-bands, used here is presented in Table 5. With this data-set, we wish to perform an SED fitting, in order to constrain properties such as stellar mass M_* , dust content A_V , metallicity and age of the LEGOs. Only one of our candidates (LEGO_GOODS-S#16) is detected in bands other than the HST bands. This object is especially interesting as its SED is extremely red. It is excluded from the SED fitting, and is discussed in Section 5.3. For the rest of the sample, the LEGOs are only detected in the HST bands and hence we choose to stack the entire sample of 23 candidates. We can then draw conclusions on the general properties of this type of object. After stacking, we

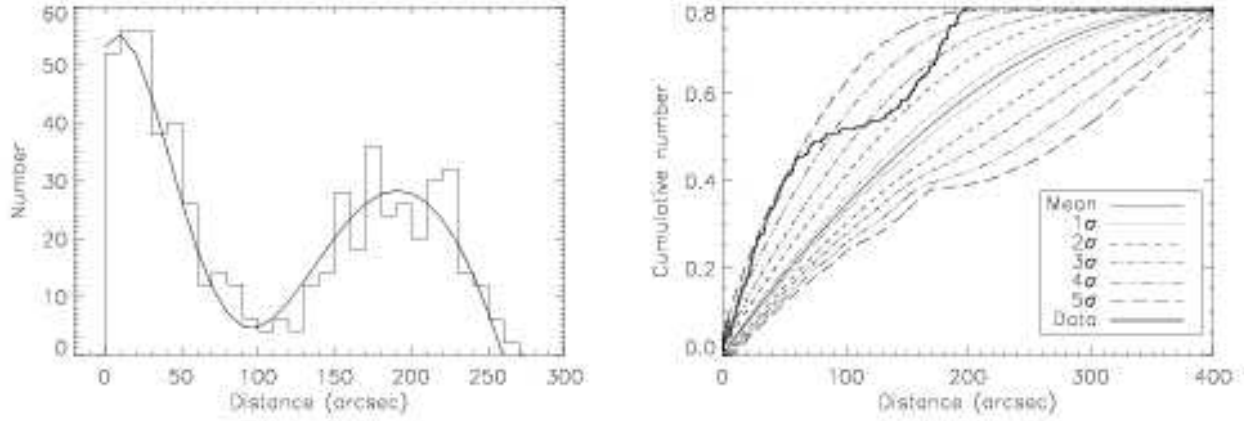


Fig. 7. *Left* Histogram distribution of distances between candidate objects in the x-direction, after re-alignment by 2.1° . Histogram is binned over 50 pixels. Solid curve is a double Gaussian fit to the data. *Right* Kolmogorov-Smirnov test of the distribution. Lines mark the simulated mean, and the $1 - 5\sigma$ contours. Thick line represents our data.

Table 5. Deep, multi-wavelength data available in the GOODS-S field. The fifth column refers to the 3σ detection limit in the sky in a $2 \times$ FWHM diameter aperture. The last column gives the 3σ detection limit as measured in a $2''$ radius aperture.

| Filter/Channel | λ_c | FWHM | Aperture radius (arcsec) | Aperture correction | 3σ limit ($2 \times$ FWHM aperture) ($\text{erg} \cdot \text{cm}^{-2} \cdot \text{s}^{-1} \cdot \text{Hz}^{-1}$) | 3σ limit ($2''$ aperture) ($\text{erg} \cdot \text{cm}^{-2} \cdot \text{s}^{-1} \cdot \text{Hz}^{-1}$) |
|-------------------------------|--------------------|--------------------|-----------------------------|------------------------|---|---|
| X-rays (<i>Chandra</i>) | 4.15 keV | 3.85 keV | 2.25 | — | $9.90 \cdot 10^{-34}$ | $9.90 \cdot 10^{-34}$ |
| U (<i>ESO 2.2-m</i>) | 3630 Å | 760 Å | 3.00 | — | $1.10 \cdot 10^{-30}$ | $8.62 \cdot 10^{-31}$ |
| B (F435W, <i>HST</i>) | 4297 Å | 1038 Å | 0.12 | 1.20 | $7.09 \cdot 10^{-32}$ | $9.25 \cdot 10^{-30}$ |
| V (F606W, <i>HST</i>) | 5907 Å | 2342 Å | 0.12 | 1.18 | $4.02 \cdot 10^{-32}$ | $4.66 \cdot 10^{-30}$ |
| i (F814W, <i>HST</i>) | 7764 Å | 1528 Å | 0.12 | 1.25 | $1.25 \cdot 10^{-31}$ | $1.50 \cdot 10^{-29}$ |
| z' (F850LP, <i>HST</i>) | 9445 Å | 1230 Å | 0.12 | 1.34 | $1.88 \cdot 10^{-31}$ | $3.00 \cdot 10^{-29}$ |
| J (<i>VLT</i>) | $1.25 \mu\text{m}$ | $0.6 \mu\text{m}$ | 0.60 | 1.22 | $1.78 \cdot 10^{-30}$ | $5.31 \cdot 10^{-30}$ |
| H (<i>VLT</i>) | $1.65 \mu\text{m}$ | $0.6 \mu\text{m}$ | 0.60 | 1.21 | $4.11 \cdot 10^{-30}$ | $1.86 \cdot 10^{-29}$ |
| K _s (<i>VLT</i>) | $2.16 \mu\text{m}$ | $0.6 \mu\text{m}$ | 0.60 | 1.37 | $4.06 \cdot 10^{-30}$ | $1.56 \cdot 10^{-29}$ |
| Ch1 (<i>Spitzer</i>) | $3.58 \mu\text{m}$ | $0.75 \mu\text{m}$ | 1.30 | 2.41 | $1.14 \cdot 10^{-31}$ | $2.36 \cdot 10^{-30}$ |
| Ch2 (<i>Spitzer</i>) | $4.50 \mu\text{m}$ | $1.02 \mu\text{m}$ | 1.80 | 1.98 | $2.07 \cdot 10^{-32}$ | $2.07 \cdot 10^{-30}$ |
| Ch3 (<i>Spitzer</i>) | $5.80 \mu\text{m}$ | $1.43 \mu\text{m}$ | 1.80 | 1.60 | $7.50 \cdot 10^{-29}$ | $7.50 \cdot 10^{-30}$ |
| Ch4 (<i>Spitzer</i>) | $8.00 \mu\text{m}$ | $2.91 \mu\text{m}$ | 2.10 | 1.85 | $6.87 \cdot 10^{-30}$ | $6.87 \cdot 10^{-30}$ |
| MIPS (<i>Spitzer</i>) | $24.0 \mu\text{m}$ | $4.70 \mu\text{m}$ | 6.00 | — | $1.23 \cdot 10^{-28}$ | $2.12 \cdot 10^{-29}$ |

get a faint detection in the K_s band. The stacked magnitudes are given in Table 6. The lack of X-ray, MIPS $24\mu\text{m}$ and radio detections (no counterparts to any of our candidates to a 3σ limit of $24 \mu\text{Jy}$, Kellermann et al. in preparation) indicates that the AGN fraction among these objects is low.

5.1. Fitting method

We used the GALAXEV code (Bruzual & Charlot, 2003) to simulate composite stellar populations, in order to fit the stacked SED of the LEGOs. The fitting was performed according to a Monte Carlo Markov Chain method (see e.g. Gilks et al. 1995 for an introduction). In outline, the method works as follows; an initial set of parameter values is chosen according to a uniform, random and logarithmic distribution within the allowed parameter space. A summary of the parameter space is given in Table 7. Given the set of parameters, a corresponding χ^2 value is calculated by running the GALAXEV code, creating a high-resolution spectrum with 6900 wavelength points from 91 \AA to $160 \mu\text{m}$. To obtain the magnitudes in each band, we apply the transmission

Table 6. Stacked magnitudes for the GOODS-S Ly α -emitters. Errors in the HST magnitudes were set to a conservative value of 0.08. Upper limits are 3σ .

| Band | Centr. Wavelength (Å) | Obs. Magnitude | Mag. Error |
|----------------|-----------------------|----------------|------------|
| U | 3710 | > 25.95 | — |
| B | 4297 | 27.57 | 0.08 |
| N | 5055 | 24.96 | 0.08 |
| V | 5907 | 26.74 | 0.08 |
| i | 7764 | 26.52 | 0.08 |
| z | 9445 | 26.56 | 0.08 |
| J | 12500 | > 26.28 | — |
| H | 16500 | > 25.55 | — |
| K _s | 21500 | 25.26 | 0.29 |
| Ch1 | 35800 | > 23.06 | — |
| Ch2 | 45200 | > 23.62 | — |
| Ch3 | 57200 | > 24.37 | — |
| Ch4 | 79000 | > 23.84 | — |

curves for the filters of the various observed wavebands; U, B,

Table 7. Parameter space sampled during the SED fitting. Metallicity is allowed to have three different values ($Z/Z_{\odot} = 0.005, 0.2$ or 1.0). The dust components are the two components of the Charlot & Fall (2000) dust model used by GALAXEV. We fit the SED with a constant star forming model, where the star formation rate in solar masses per year is given by “SF-rate”.

| Parameter | Min. value | Max. value |
|-------------------------------|------------|------------|
| Metallicity (Z/Z_{\odot}) | 0.005 | 1.0 |
| Dust- τ | 0 | 4 |
| Dust- μ | 0 | 1 |
| SF-rate | 0.01 | 100 |
| Age (Gyrs) | 0.001 | 1.5 |

V, i, z', J, H, K_s and the four Spitzer bands, $Ch1-Ch4$. In this analysis, we exclude the Spitzer *MIPS* band as it is very difficult to stack images in this band because of the source confusion. At this redshift, the *MIPS* band is also contaminated by a PAH emission feature. We then normalise the output spectrum so that the magnitude in the model z' -band equals that of the observed z' -band. The χ^2 is then calculated by comparing the magnitudes in all the other bands. We incorporate points with upper limits in the following way; if the predicted flux lies below the upper limit, no value is added to the total χ^2 , if the predicted flux lies above the observed one, a χ^2 is added, assuming the error on the upper limit is 0.1 in magnitude. Hence, models with flux above the upper limit may be acceptable if the flux in this band is only slightly above the limit. In most cases though, the model will be rejected due to high χ^2 .

Once the χ^2 has been calculated for a particular model, a new random set of parameters is chosen, by adding a “step vector”. The step size in each parameter is chosen randomly in a logarithmic interval between 1% and 100% of the total size of the parameter space. This step vector is equally likely to be positive or negative. The choice of logarithmic step sizes is a natural choice if no assumptions about the scale of change that affect the solution are to be made and ensures a fast convergence. When a step has been calculated and the new parameters have been calculated, the new model is accepted into the chain with a probability proportional to the exponential difference between the old and new χ^2 . If the new model is accepted, it is added as the next step in the chain, i.e. the parameters of that particular model are printed in the output file. If the model is not accepted, a copy of the old parameters is added as the next step. This procedure is repeated until a chain with 30000 elements has been created. The independence of individual steps in the walk ensures that the resulting chain is Markovian in character, i.e. that the resulting chain after many iterations is a representation of the full probability distribution function in the chosen parameter space. The output file can then be used to study the distribution in each parameter, and to determine the mean and the confidence levels within each parameter. It can also be used to study dependencies between parameters, such as e.g. in Fig. 8.

5.2. Results from SED fitting

The parameters we wish to fit are stellar mass, dust content, star formation rate, metallicity and age. Redshift is set to be the central Ly α redshift of the narrow-band filter, i.e. $z = 3.15$. We use the Salpeter initial mass function (IMF) from 0.1 to $100 M_{\odot}$ and the extinction law of Charlot & Fall (2000). We also incorporate the effect of the Ly α forest according to the model of Madau

(1995). We use constant star formation histories. The metallicity was allowed to be either $Z/Z_{\odot} = 0.005, 0.2$ or 1.0 . Of the 30000 runs, 73% were with the lowest metallicity, 21% with the medium metallicity and 6% had solar metallicity. Hence the best fit models have a very low metallicity. For the rest of the analysis, we choose to only look at the models which have the lowest metallicity, as these models seem to be preferred. For these models, the best fit parameters are $M_* = 4.7^{+4.2}_{-3.2} \times 10^8 M_{\odot}$, age = $0.85^{+0.13}_{-0.42}$ Gyrs, $A_V = 0.26^{+0.11}_{-0.17}$, and star formation rate SFR = $0.66^{+0.51}_{-0.31} M_{\odot} \text{ yr}^{-1}$, where the errors are 1σ . Contour-plots of the three parameters mass, age and dust are shown in Fig. 8. The degeneracies between the different parameters can

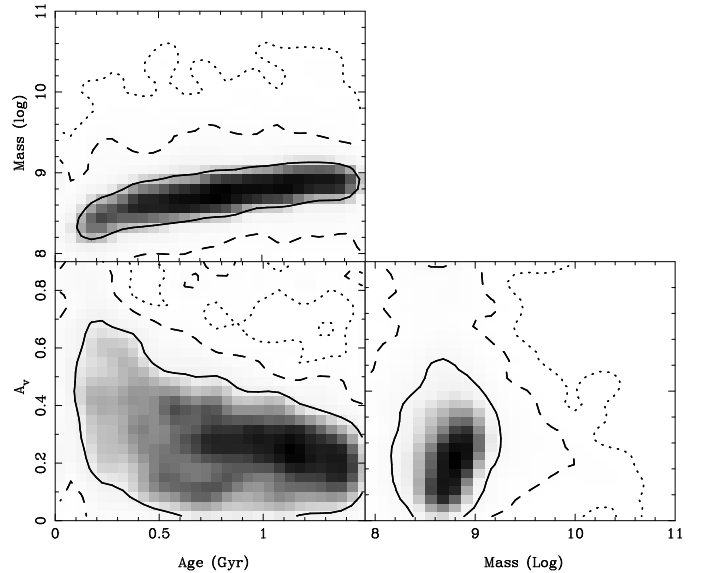


Fig. 8. Contour-plots of the mass, age and dust parameters in our SED fitting. Contours indicate 1, 2 and 3σ levels.

be seen. In Fig. 9, the weighted GALAXEV spectrum of a subset of 10 models with $\chi^2 \sim 1$ is shown with the measured SED overplotted. The *U*-band and Spitzer/IRAC data are too shallow to be useful in constraining the data, and the narrow-band data-point is plotted only for reference.

5.3. Object LEGO_GOODS-S#16

One candidate emission line object, LEGO_GOODS-S#16, was detected in all available GOODS-S bands, except the *U* and *B* bands, and in X-rays. The fluxes of the object can be found in Table 8, and the thumb-nail images seen in Fig. 10. As there is significant excess emission in our narrow-band filter, we expect the source to be either an [OII]-emitter at $z = 0.36$ or a Ly α -emitter at $z = 3.15$. This object was first fit with the same type of stellar SED as the other sample, but with the redshift set to be either $z = 0.36$ if the narrow-band emission is [OII] or $z = 3.15$ if the emission is Ly α . This fitting yielded no good fit, with $\chi^2 \gtrsim 500$.

Two types of objects could show MIR colours similar to those of this galaxy; *i*) obscured AGNs (e.g. Lacy et al. 2004; Stern et al. 2005) and *ii*) ULIRG/dusty starburst galaxies (e.g. Ivison et al. 2000; Klaas et al. 2001). The infrared colours can be plotted in the diagnostic colour-colour diagram of Ivison et al. (2004), see Fig. 11. In this diagram, Ivison et al. (2004) plot

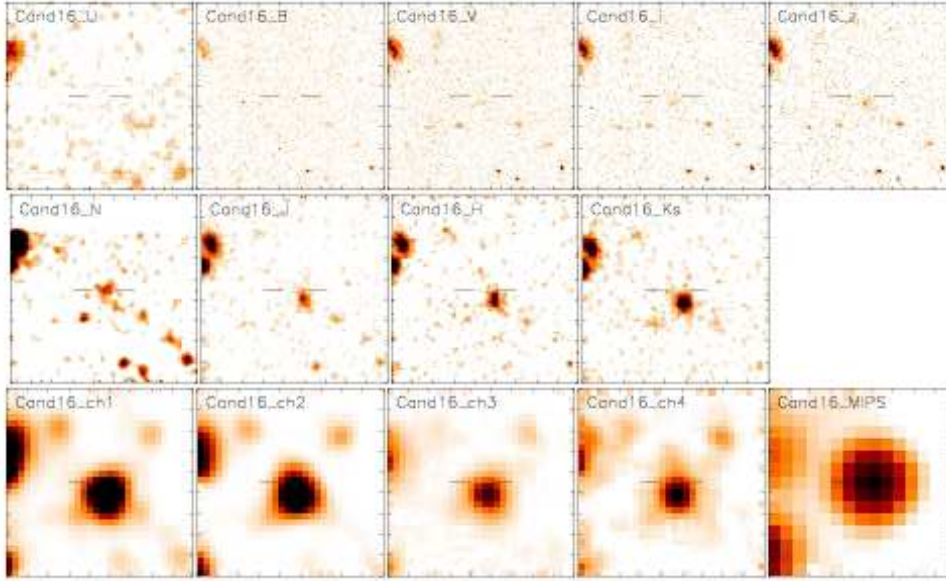


Fig. 10. Thumb-nail images, $18''$ across, of LEGO_GOODS-S#16.

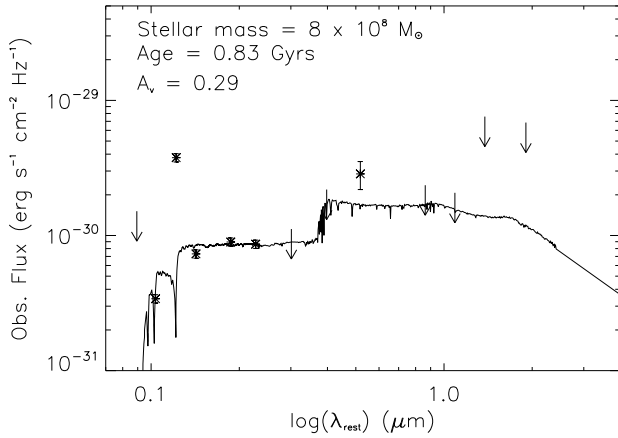


Fig. 9. The average spectrum of 10 models with $\chi^2 \sim 1$. The spectrum is calculated by 1) creating the 10 spectra with the particular parameters of the models with GALAXEV, 2) averaging the 10 spectra together, weighted with the χ^2 , so that the total flux density is $F_\nu = [\sum_i F_\nu^i \times (1/\chi_i^2)] / \sum_i (1/\chi_i^2)$. The parameters of the model spectrum are as indicated on the plot. They are the weighted average parameters of the 10 models used, weighted in the same way as the spectra. Data points from stacked SED. Upper limits are represented with arrows. The point well off the SED is the narrow-band magnitude.

the colours of Arp 220, Mrk 231 and a theoretical starburst spectrum as observed at different redshifts. The comparison with the colours of LEGO_GOODS-S#16 shows the object to be more likely a low-redshift starburst galaxy. However, Ivison et al. (2004) do not take PAH emission into account. The most important PAH lines are at 3.3, 6.2, 7.7, 8.7, and $11.2 \mu\text{m}$ (corresponding to 13.7, 25.7, 32.0, 36.1, 46.5 at $z = 3.15$). Especially the second line falls on top of the MIPS $24 \mu\text{m}$ band. This would explain the extreme rise in flux in this band. In Fig. 12, we see

Table 8. SED of object LEGO_GOODS-S#16. Upper limit is 3σ . Continuum sources are offset from the narrow-band source by approximately 0.8 arcseconds, corresponding to 5.9 kpc at $z = 3.15$.

| Band | Centr. Wavelength (μm) | Obs. flux (μJy) | Flux Error (μJy) |
|----------|-------------------------------------|------------------------------|-------------------------------|
| B | 0.430 | > 0.03 | — |
| NB | 0.506 | 0.39 | 0.042 |
| V | 0.591 | 0.06 | 0.008 |
| <i>i</i> | 0.776 | 0.13 | 0.010 |
| <i>z</i> | 0.945 | 0.24 | 0.018 |
| J | 1.25 | 3.47 | 0.157 |
| H | 1.65 | 7.40 | 0.420 |
| Ks | 2.15 | 12.51 | 0.565 |
| Ch1 | 3.58 | 24.87 | 0.188 |
| Ch2 | 4.50 | 30.86 | 0.200 |
| Ch3 | 5.80 | 31.85 | 0.710 |
| Ch4 | 8.00 | 21.31 | 0.990 |
| MIPS | 24.00 | 271.11 | 7.001 |

that this emission could easily add a factor of ten to the flux in this band, hence the $24 \mu\text{m}/8 \mu\text{m}$ colour of LEGO_GOODS-S#16 can be adjusted downwards by a factor of ten. The extra line emission explains why a $z \sim 3$ star-burst galaxy would appear to be at lower redshifts. To understand if this is a low or high redshift object, we have also attempted to get a photometric redshift estimate for this galaxy using the *HyperZ* code (Bolzonella et al. 2000), both with and without including the Spitzer data points. The results were similar for both cases. When we do not include the Spitzer data, the best fit is redshift $z = 1.7$ with a χ^2 of approximately 8. For the redshift $z = 0.4$, the fit then has a $\chi^2 \approx 126$ and for the Ly α redshift of $z = 3.15$, the $\chi^2 \approx 35$. When the Spitzer points are included, the higher redshift is even more favoured. Hence, it seems unlikely that this is a lower redshift source.

We wish to distinguish whether LEGO_GOODS-S#16 is an obscured AGN or a starburst galaxy. Several papers have presented infrared colours for obscured (and unobscured) AGN (Johansson et al. 2004; Lacy et al. 2004; Stern et al. 2005;

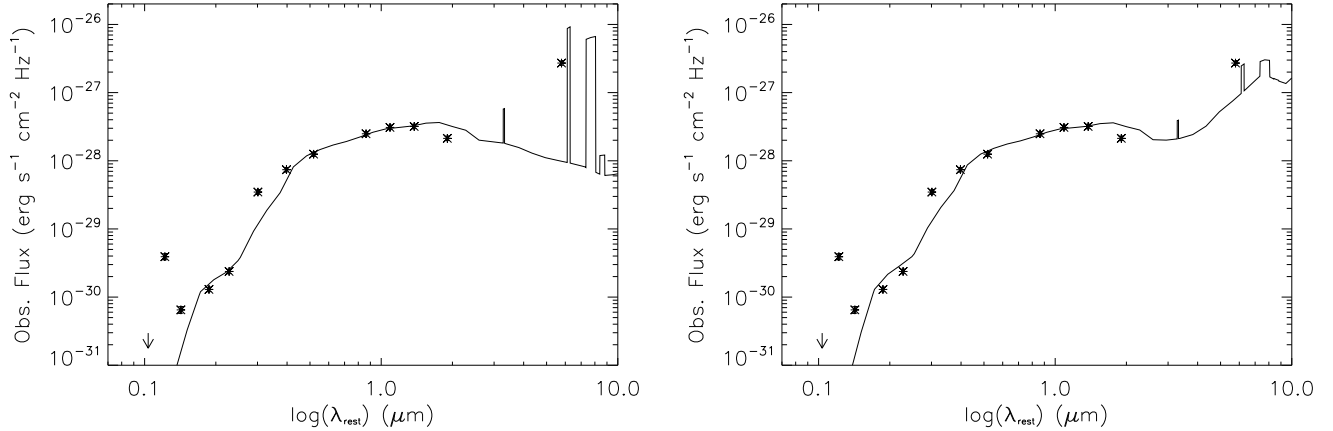


Fig. 12. Two preliminary GRASIL model fits to the SED of LEGO_GOODS-S#16, both with $\chi^2 \sim 50$. Points with error bars (of the same size as the point) are our data, with errors being purely statistical. The point off the curve at lower wavelengths is the narrow-band detection.

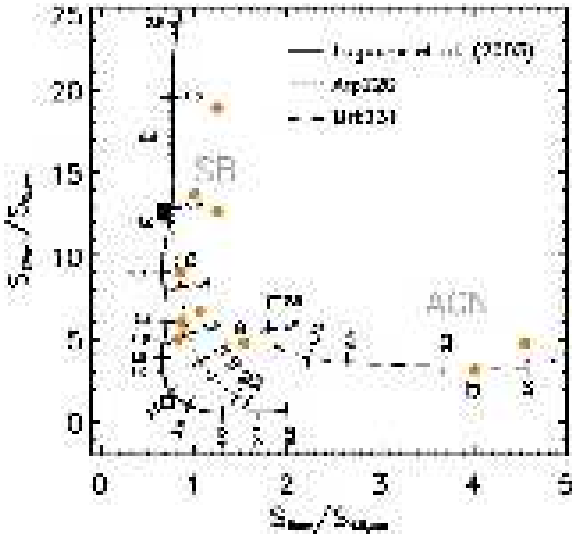


Fig. 11. Diagram of Ivison et al. (2004). The x- and y-axes show the colours in the Spitzer bands and the solid lines mark the locations of AGN and starburst galaxies (SB) depending on redshift. The redshifts are marked along the lines. The orange dots mark the location of a set of sub-mm galaxies presented in Ivison et al. (2004). The solid square marks the location of the colours of LEGO_GOODS-S#16, indicating a lower redshift starburst galaxy. The open square marks the colours of this galaxy if the MIPS 24 μm flux is decreased by a factor of 10 (see text). This point is indicative of a redshift $z \sim 3$ starburst galaxy.

Alonso-Herrero et al. 2006) and especially two papers publish selection criteria for obscured AGNs (Lacy et al. 2004; Stern et al. 2005). The colours of LEGO_GOODS-S#16 are inconsistent with those selection criteria and we therefore rule out an AGN nature of this galaxy. This conclusion is further supported by the non-detection in X-rays. In order to study if the SED of the galaxy could be fitted by a starburst spectrum, we tried to fit the SED with a GRASIL (Silva et al. 1998) model of a starburst galaxy. GRASIL is a spectral stellar synthesis code, which takes into account the dust obscuration of starlight in both molecular

clouds and the diffuse medium. Hence it is perfectly suited for the investigation of starburst galaxies. We could fit the photometric data of LEGO_GOODS-S#16 by a relatively old burst (~ 1 Gyr) at $z = 3.15$ with a significant amount of dust. The results are shown in Fig. 12. As can be seen in the Figure, these models reproduce the trends in the observed SED relatively well. This appears to be a redshift $z = 3.15$ dusty starburst galaxy, with a region where the dust amount is smaller and Ly α emission can escape, offset from the central parts of the galaxy. It would be of great interest to get sub-mm imaging of this object in order to constrain the SED better.

6. Comparison to Lyman-Break Galaxies

We wish to compare our sample of LEGOs to a sample of faint Lyman Break Galaxies (LBGs) in order to determine the similarities and differences of the two populations of high-redshift galaxies. First, we want to know if our LEGOs would be detected as LBGs and so we apply the LBG selection criteria for U -band drop-outs of Wadadekar et al. (2006; $U - B > 1.0$, $U - B > B - V + 1.3$ and $B - V < 1.2$) as well as the criteria of Madau et al. (1996; $U - B > 1.3$, $U - B > B - i + 1.2$ and $B - i < 1.5$) to our sample. However, our U -band data, and in the case of the faintest candidates also the HST data, is too shallow to get a useful measurement on the $U - B$ colour. Instead, we take the best fit spectrum from the SED fitting (see Fig. 9) and convolve it with the U (F300W), B and V filter sensitivities and calculate the colours. For this model spectrum, these colours become $U - B = 4.51$, $B - V = 0.24$ and $B - i = 0.69$ which well satisfy the selection criteria for U -band drop-outs, see Fig. 13. However, many of our LEGOs are very faint and the stacked B magnitude is fainter than the lower limit of the selection of Madau et al. (1996), and about half of our sample are fainter than the V cut-off in the sample of Wadadekar et al. (2006), see Fig. 14.

Secondly, we wish to compare the observed optical colours (restframe UV colours) of our LEGOs to the LBGs in order to establish if our LEGO candidates have the same UV continuum colours as LBGs on the red side of the Lyman break. In Fig. 14, we plot the colours of the two samples of faint LBGs published by Wadadekar et al. (2006) and Madau et al. (1996) against the

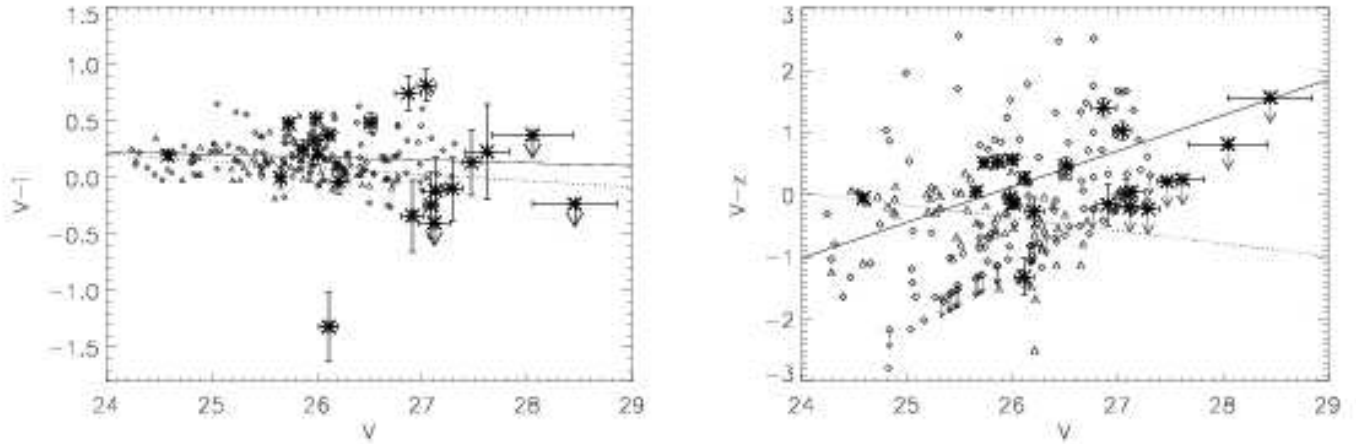


Fig. 14. Colours of our candidates (stars with error bars) compared to colours of the sample of faint LBGs of Wadadekar et al. (2006; diamonds) and Madau et al. (1996; triangles). Lines represent the best fit to the LBG data, the solid line the fit to the sample by Wadadekar et al. (2006) and the dotted line the fit to the Madau et al. (1996) sample. *Left* V minus i colours, *Right* V minus z' colours. Small arrows indicate upper limits for the Wadadekar et al. (2006) sample.

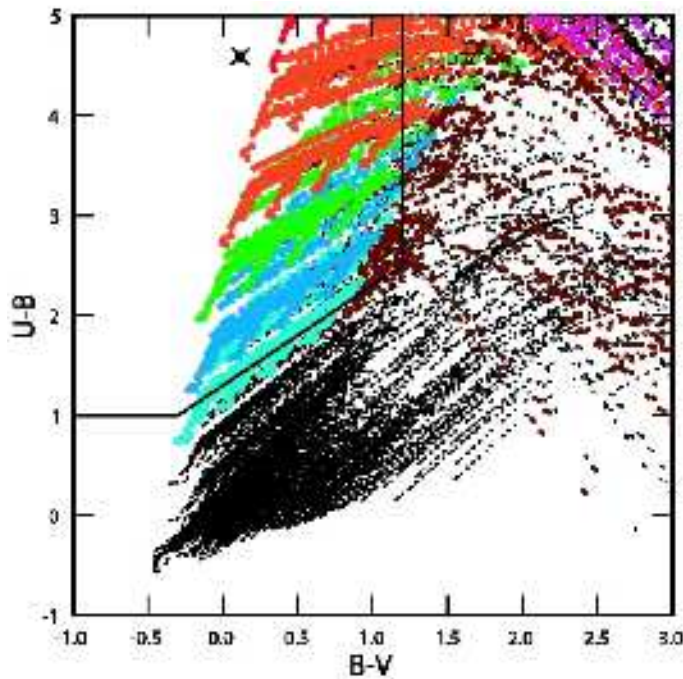


Fig. 13. Colour-colour plot from Wadadekar et al. (2006) showing simulated galaxy colours, see that paper for details. The solid line marks the area (upper left corner) where redshift $z \approx 3$ LBG reside. The large star in the upper left corner marks the colours of our best-fit synthetic model, well within the selection boundaries for high-redshift LBGs.

colours of our candidates. All samples are drawn from survey data-sets such as GOODS-S and HDF-N, hence there is no bias in photometry. In the plot, we see that the LEGO candidates are drawn from a fainter sub-sample of the high-redshift galaxy population. However, for the brighter candidates among our sample, the LEGOs appear to have UV colours similar to LBG galaxies.

7. Conclusion

We have performed deep narrow-band imaging of part of the GOODS-S field. The image revealed a set of 24 LEGO candidates, at a redshift of $z \approx 3.15$. Of these, three candidates have been observed spectroscopically and are confirmed. The spatial distribution of the candidates appear to be in a filamentary structure, with a 4σ confidence, however to confirm this and to plot the filament in 3D-space, we would need spectroscopic redshifts. We have studied the entire candidate sample in all bands available from X-rays to infrared in the GOODS-S data-set. From the SED fitting we conclude that the LEGOs on average have low metallicity ($Z/Z_{\odot} = 0.005$), have stellar masses in the range of $1 - 5 \times 10^9 M_{\odot}$ and low dust extinction ($A_V \sim 0.3$). The candidates have ages in the range of 100 – 900 Myrs. We also find one galaxy, LEGO_GOODS-S#16, which is best fit by a dusty starburst galaxy at $z = 3.15$ with Ly α -emission escaping from an area slightly offset from the central core.

The comparison to a sample of U -band drop-out galaxies in the GOODS-S field show that the colours of LEGOs are consistent with the selection criteria for U -band drop-outs except they are too faint to be detected from their continuum flux. They also have colours similar to those of LBGs at redshift $z \approx 3$. In agreement with previous results (e.g. Gawiser et al. 2006), we conclude that Ly α -emitters at redshift $z \sim 3.1$ are dust- and AGN-free, star-forming galaxies with small to medium masses.

Acknowledgements. KN and KP gratefully acknowledges support from IDA – Instrumentcenter for Danish Astrophysics. The Dark Cosmology Centre is funded by the DNRF. The authors thank the DDT panel and the ESO Director General for granting time for follow-up spectroscopy. KN wishes to thank Matthew Hayes and Christian Tapken for interesting discussions and comments on the manuscript. LFG acknowledges financial support from the Danish Natural Sciences Research Council.

References

- Alonso-Herrero, A., Pérez-González, P.G., Alexander, D.M., et al., 2006, ApJ, 640, 167
- Bertin, E., Arnouts, S. 1996, A&AS, 117, 393
- Bolzonella, M., Miralles, J.-M., Pelló, R., 2000, A&A 363, 476
- Brocklehurst, M., 1971, MNRAS, 153, 471
- Bruzual G.A., Charlot S., 2003, MNRAS, 344, 1000

- Chapman S.C., Scott D., Windhorst R.A. et al., 2004, *ApJ*, 606, 85
- Charlot, S., & Fall, S.M., 2000, *ApJ*, 539, 718
- Cowie, L.L., & Hu, E.M., 1998, *AJ*, 115, 1319
- Dey A., Bian C., Soifer B.T. et al., 2005, *ApJ*, 629, 654
- Francis, P.J., Woodgate, B.E., Warren, S.J. et al., 1996, *ApJ*, 457, 490
- Francis P.J., Williger G.M., Collins N.R. et al., 2001, *ApJ*, 554, 1001
- Freedman, W.L., Madore, B.F., Gibson, B.K., et al., 2001, *ApJ*, 553, 47
- Fruchter, A. S., Levan, A. J., Strolger, L. et al., 2006, *Nature*, 441, 463
- Fujita, S.S., Ajiki, M., Shioya, Y., et al., 2003, *AJ*, 125, 13
- Furlanetto, S.R., Schaye, J., Springel, V., & Hernquist, L., 2003, *ApJ*, 599, L1
- Fynbo, J.P.U., Møller, P., & Warren, S.J. 1999, *MNRAS*, 305, 849
- Fynbo, J.P.U., Møller, P., & Thomsen, B. 2001, *A&A* 374, 443
- Fynbo, J.P.U., Ledoux, C., Møller, P., Thomsen, B., & Burud, I., 2003, *A&A*, 407, 147
- Fynbo, J.P.U., Gorosabel, J., Smette, A., et al., 2005, *ApJ*, 633, 317
- Gawiser, E., Van Dokkum, P.G., Gronwall, C., et al., 2006, *ApJL*, 642, 13
- Giavalisco, M., Ferguson, H.C., Koekemoer, A.M., et al., 2004, *ApJ*, 600, L93
- Gilks, W.R., Richardson, S., & Spiegelhalter, D.J., 1995, *Markov Chain Monte Carlo in Practice*, Chapman & Hall, ISBN 0412055511
- Hayashino, T., Matsuda, Y., Tamura, H., et al., 2004, *AJ*, 128, 2073
- Hayes, M., & Östlin, G., 2006, *A&A*, 460, 681
- Hu, E.M., & McMahon, R.G., 1996, *Nature*, 382, 231
- Iverson, R.J., Smail, I., Barger, A.J., et al., 2000, *MNRAS*, 315, 209
- Iverson, R.J., Greve, T.R., Serjeant, S. et al., 2004, *ApJS*, 154, 124
- Jaunsen, A.O., Andersen, M.I., Hjorth, J., et al., 2003, *A&A*, 402, 125
- Johansson, P.H., Väisänen, P., & Vaccari, M., 2004, *A&A*, 427, 795
- Keel W.C., Cohen S.H., Windhorst R.A., Waddington I., 1999, *AJ*, 118, 2547
- Kennicutt, R.C., 1983, *ApJ*, 272, 54
- Klaas, U., Haas, M., Müller, S.A.H., et al., 2001, *A&A*, 379, 823
- Lacy, M., Storrie-Lombardi, L.J., Sajina, A., et al., 2004, *ApJS*, 154, 166
- Leitherer, C., Schaerer, D., Goldader, J.D., et al., 1999, *ApJS*, 123, 3
- Lowenthal, J. D., Hogan, C. J., Green, R. F., et al., 1991, *ApJ*, 377, L73
- Madau, P., 1995, *ApJ*, 441, 18
- Madau, P., Ferguson, H.C., Dickinson, M.E., et al., 1996, *MNRAS*, 283, 1388
- Malhotra, S., & Rhoads, J.E. 2002, *ApJL*, 565, L71
- Matsuda Y., Yamada T., Hayashino T. et al., 2004, *AJ*, 128, 569
- Matsuda, Y., Yamada, T., Hayashino, T. et al., 2005, *ApJ*, 634, L125
- Monaco, P., Møller, P., Fynbo, J.P.U., et al., 2005, *A&A*, 440, 799
- Møller, P., & Warren, S.J. 1993, *A&A* 270, 43
- Møller P., & Warren S.J. 1998, *MNRAS* 299, 661
- Møller, P., & Fynbo, J.U. 2001, *A&A*, 372, L57
- Møller, P., Warren, S.J., Fall, S. M., Fynbo, J.U., & Jakobsen, P. 2002, *ApJ*, 574, 51
- Nilsson, K., Fynbo, J.P.U., Møller, P., Sommer-Larsen, J., & Ledoux, C., 2006, *A&A* 452, L23
- Ouchi, M., Shimasaku, K., Furusawa, H. et al., 2003, *ApJ*, 582, 60
- Ouchi, M., Shimasaku, K., Okamura, S. et al., 2004, *ApJ*, 611, 685
- Overzier, R.A., Miley, G.K., Bouwens, R.J., et al., 2006, *ApJ*, 637, 58
- Palunas P., Teplitz H.I., Francis P.J., Williger G.M., Woodgate B.E., 2004, *ApJ*, 602, 545
- Partridge, R.B., & Peebles, P.J.E., 1967, *ApJ*, 147, 868
- Pascarelle, S.M., Windhorst, R.A., Driver, S.P., Ostrander, E.J., & Keel, W.C., 1996, *ApJ*, 456, L21
- Peacock, J.A., 1983, *MNRAS*, 202, 615
- Petitjean, P., Pecontal, E., Valls-Gabaud, D., & Charlot, S., 1996, *Nature*, 380, 411
- Pritchett, C.J., 1994, *PASP*, 106, 1052
- Pope, A., Borys, C., Scott, D., et al., 2005, *MNRAS*, 358, 149
- Schaerer, D., & Pelló, R., 2005, *MNRAS*, 362, 1054
- Schmitt, H.R., Calzetti, D., Armus, L., et al., 2006, *ApJ*, 643, 173
- Silva, L., Granato, G.L., Bressan, A., & Danese, L., 1998, *ApJ*, 509, 103
- Smail, I., Chapman, S.C., Blain, A.W., & Ivison, R.J., 2004, *ApJ*, 616, 71
- Steidel, C.C., Adelberger, K.L., Giavalisco, M., Dickinson, M., & Pettini, M., 1999, *ApJ*, 519, 1
- Steidel, C.C., Adelberger, K., Shapley, A.E., et al., 2000, *ApJ*, 532, 170
- Stern, D., Eisenhardt, P., Gorjian, V., et al., 2005, *ApJ*, 631, 163
- Venemans, B.P., Röttgering, H.J.A., Miley, G.K. et al., 2005, *A&A*, 431, 793
- Wadadekar, Y., Casertano, S., & de Mello, D., 2006, *AJ*, 132, 1023
- Wang, J.X., Rhoads, J.E., Malhotra, S., et al., 2004, *ApJL*, 608, 21
- Warren, S.J., & Møller, P., 1996, *A&A*, 311, 25
- Warren, S.J., Møller, P., Fall, S.M., & Jakobsen, P., 2001, *MNRAS*, 326, 759
- Weidinger, M., Møller, P., Fynbo, J.P.U., Thomsen, B., & Egholm, M.P. 2002, *A&A*, 391, 13
- Wolfe, A.M., Turnshek, D.A., Smith, H.E., & Cohen, R.D., 1986, *ApJS*, 61, 249
- Wolfe, A.M., Gawiser, E., & Prochaska, J.X., 2005, *ARAA*, 43, 861